



ARRCI  
J

# Selective Uptake and Imaging of Aptamer- and Antibody-Conjugated Hollow Nanospheres Targeted to Epidermal Growth Factor Receptors Overexpressed in Head and Neck Cancer

Marites Pasuelo Melancon,<sup>†</sup> Min Zhou,<sup>‡</sup> Rui Zhang,<sup>‡</sup> Chiyi Xiong,<sup>‡</sup> Peter Allen,<sup>§</sup> Xiaoxia Wen,<sup>‡</sup> Qian Huang,<sup>‡</sup> Michael Wallace,<sup>†</sup> Jeffrey N. Myers,<sup>||</sup> R. Jason Stafford,<sup>†</sup> Dong Liang,<sup>#</sup> Andrew D. Ellington,<sup>§</sup> and Chun Li<sup>‡,\*</sup>

<sup>†</sup>Departments of Interventional Radiology, <sup>‡</sup>Cancer Systems Imaging, <sup>||</sup>Head and Neck Surgery, and <sup>†</sup>Imaging Physics, The University of Texas MD Anderson Cancer Center, 1515 Holcombe Boulevard, Houston, Texas 77030, United States, <sup>§</sup>Department of Chemistry and Biochemistry, The University of Texas at Austin, 1 University Station, Austin, Texas 78712, United States, and <sup>#</sup>Department of Pharmaceutical Sciences, Texas Southern University, 3100 Cleburne Street, Houston, Texas 77004, United States

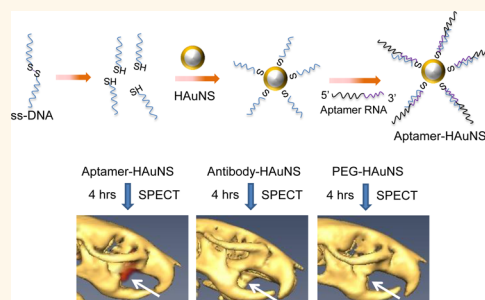
**ABSTRACT** The purpose of this study was to compare the binding affinity and selective targeting of aptamer- and antibody-coated hollow gold nanospheres (HAuNS) targeted to epidermal growth factor receptors (EGFR). EGFR-targeting aptamers were conjugated to HAuNS (apt-HAuNS) by attaching a thiol-terminated single-stranded DNA to the HAuNS and then adding the complementary RNA targeted to EGFR. Apt-HAuNS was characterized in terms of size, surface charge, absorption, and number of aptamers per particle. The *in vivo* pharmacokinetics, *in vivo* biodistribution, and micro-SPECT/CT imaging of <sup>111</sup>In-labeled apt-HAuNS and anti-EGFR antibody (C225)-conjugated HAuNS were evaluated in nude mice bearing highly malignant human OSC-19 oral tumors.

<sup>111</sup>In-labeled PEG-HAuNS was used as a control ( $n = 5$ /group). Apt-HAuNS did not have an altered absorbance profile or size ( $\lambda_{\text{max}} = 800 \text{ nm}$ ; diameter = 55 nm) compared to C225-HAuNS or PEG-HAuNS. The surface charge became more negative upon conjugation of the aptamer (-51.4 vs -19.0 for PEG-HAuNS and -25.0 for C225-HAuNS). The number of aptamers/particle was  $\sim 250$ . *In vitro* cell binding and *in vivo* biodistribution showed selective binding of the apt-HAuNS to EGFR.  $\mu$ SPECT/CT imaging confirmed that there was more tumor uptake of apt-HAuNS than C225-HAuNS. Aptamer is a promising ligand for image-guided delivery of nanoparticles for treatment of tumor cells overexpressing EGFR.

**KEYWORDS:** hollow gold nanospheres · SPECT/CT · biodistribution · epidermal growth factor receptor · head and neck cancer · aptamer

**O**ne advantage of nanoparticles over small molecular compounds is their ability to perform multiple functions simultaneously. In particular, nanotechnology can be used to tailor treatment to individual patients by integrating diagnostic and therapeutic capabilities into a single entity. These theranostic techniques rely on the successful delivery and detection of nanoparticles at the diseased sites. Multifunctional nanomaterials that absorb light with high efficiency are especially useful for theranostic applications. These light-absorbing agents can not only reveal the molecule-specific signatures of cancer with

high sensitivity and high spatial resolution when viewed using photoacoustic imaging<sup>1,2</sup> but also mediate the selective killing of cancer cells via photothermal ablation and drug release.<sup>3</sup> Image-guided phototherapy, especially when done in real time, allows for the optimal planning of the therapy and more accurate targeting of the treatment volume and nearby critical structures. After therapy delivery, changes in parameters such as tissue perfusion and diffusion may be used to visualize the extent of therapy and thus can be used as crucial feedback regarding the safety, efficacy, and overall outcomes of the therapy.



\* Address correspondence to  
cli@mdanderson.org.

Received for review December 27, 2013  
and accepted April 22, 2014.

Published online April 22, 2014  
10.1021/nn406632u

© 2014 American Chemical Society

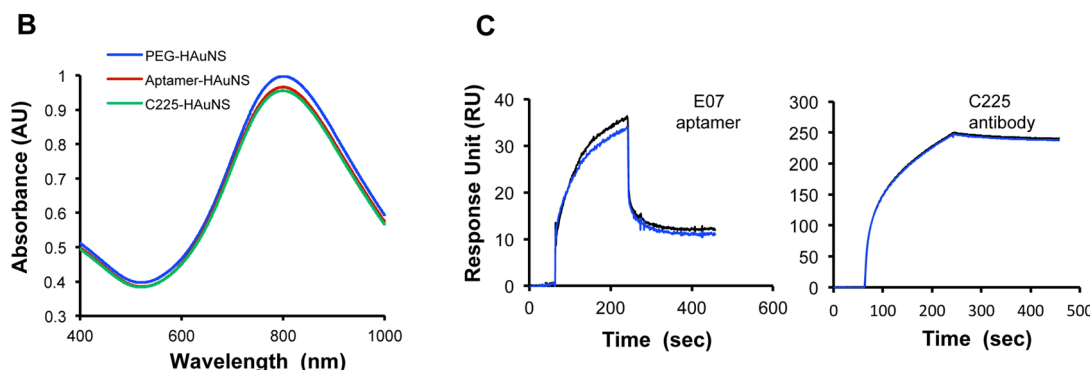
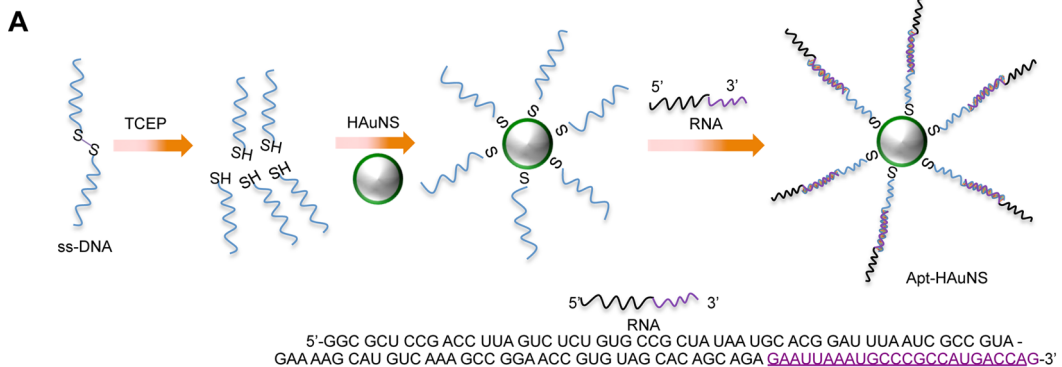


**Figure 1.** (A) Schema for the conjugation of aptamer to HAuNS. (B) Absorbance spectrum of apt-HAuNS, C225-HAuNS, and PEG-HAuNS in water, which peaked at 800 nm. (C) Representative surface plasmon resonance sensograms of aptamer and C225 antibody on sensor chips coated with rhEGFR. Each ligand was injected and analyzed in duplicate binding cycles. The vertical axes in response units represent binding of each ligand to immobilized rhEGFR.

Gold core–shell nanostructures, which consist of a dielectric or semiconducting core surrounded by an ultrathin gold shell, have been shown to mediate both photodetection and phototherapy.<sup>4,5</sup> Hollow gold nanospheres (HAuNS) are second-generation gold nanostructures that have the unique combination of small size (outer diameter = 30–50 nm), spherical shape, and hollow interior with a thin gold shell (3–6 nm). Various homing ligands, including aptamers,<sup>6</sup> peptides,<sup>7</sup> antibodies,<sup>8</sup> and small-molecular-weight organic compounds,<sup>9</sup> have been conjugated on the surface of gold nanoshells. These homing ligands selectively direct the nanoparticles to the target sites.

Aptamers consist of short DNA/RNA molecules that can bind specifically to proteins and other targets. Because of their relatively small size, high specificity, and nonimmunogenicity, they are being developed for treatment of diseases, such as cancer, HIV, heart diseases, and macular degeneration. In fact, a few aptamers are either approved by the U.S. Food and Drug Administration or are currently in clinical trials.<sup>10</sup> Several works based on aptamer with siRNA and nanoparticles are also currently being investigated in preclinical animal models for the treatment and imaging of cancer and HIV.<sup>11–13</sup> On the basis of these previous studies, we hypothesized that aptamers targeted to epidermal growth factor receptors (EGFR)

are attractive homing ligands for the targeted thermal ablation of head and neck cancers.

To compare the utility of aptamers with that of currently used ligands, we evaluated the effect of conjugating aptamers *versus* that of conjugating an antibody on the surface of HAuNS targeted to EGFR. EGFR is overexpressed in 90% of head and neck cancers;<sup>14–16</sup> the mean EGFR levels in squamous cell cancer of the head and neck and normal tissue have more than 13-fold difference.<sup>17</sup> The selective accumulation of aptamer- and antibody-conjugated HAuNS was compared on the basis of the *in vivo* pharmacokinetics and biodistribution of HAuNS in tumor-bearing mice, and the increased uptake of the HAuNS conjugates was validated using single-photon emission computed tomography/computed tomography (SPECT/CT) imaging of <sup>111</sup>In-labeled HAuNS.

## RESULTS AND DISCUSSION

**Apt-HAuNS Characterization.** Aptamers were conjugated to HAuNS by annealing SH-terminated single-stranded DNA to the HAuNS first and then adding the RNA targeted to EGFR, which has 22 bases complementary to the single-stranded DNA (Figure 1A). We found that the resulting Apt-HAuNS had a mean size of  $59.6 \pm 1.9$  nm and a zeta potential of  $-51.4 \pm 5.1$  (Table 1). The size of apt-HAuNS was comparable to that of PEG-HAuNS and C225-HAuNS, but apt-HAuNS

**TABLE 1. Physicochemical Properties of HAuNS Conjugates<sup>a</sup>**

material	PEG-HAuNS	Apt-HAuNS	C225-HAuNS
mean size, nm	55.3 ± 0.4	59.6 ± 1.9	59.2 ± 1.2
zeta potential	-19.0 ± 3.6	-51.4 ± 5.1	-25.0 ± 2.5

<sup>a</sup>The data are expressed as mean ± standard deviation ( $n = 3$ ).

was more negatively charged than PEG-HAuNS (zeta potential =  $-19.0 \pm 3.6$ ) and C225-HAuNS (zeta potential =  $-25.0 \pm 2.5$ ). The absorption spectrum for apt-HAuNS was very similar to that of PEG- and C225-conjugated HAuNS (Figure 1B), with all of the HAuNS particles having maximum absorption in the near-infrared region ( $\sim 800$  nm). These results indicate that surface modification of the HAuNS with aptamer did not significantly change the optical and size properties of the HAuNS.

Figure 1C shows a representative sensorgram obtained from SPR analyses of EGFR-targeting aptamer. The  $K_d$  values for aptamer and C225 were 112 nM ( $k_{off}/k_{on} = 1.42 \times 10^{-3} \text{ s}^{-1}/1.26 \times 10^4 \text{ M}^{-1} \text{ s}^{-1}$ ) and 1.69 nM ( $k_{off}/k_{on} = 2.58 \times 10^{-4} \text{ s}^{-1}/k_{on} = 1.53 \times 10^5 \text{ M}^{-1} \text{ s}^{-1}$ ), respectively (Figure 1C).

Quantification of the number of aptamers per particle was accomplished using gel electrophoresis (Figure 2). By calculating the signal intensity, we found that there was 1 pmol of RNA per 50  $\mu\text{L}$  of HAuNS, which is equivalent to  $\sim 250$  molecules of aptamer/particle. In comparison, approximately 124 C225 antibody molecules were attached in the C225-HAuNS.<sup>8</sup> We attributed this difference in number of ligands per particle to the smaller size of the aptamer (molecular weight = 35 kDa), which is four times smaller than C225 (molecular weight = 150 kDa).

Aptamer in apt-HAuNS was stable up to 48 h in plasma. More than 60% of intact aptamer was associated with HAuNS after 48 h incubation in 50% mouse plasma at 37 °C as revealed by electrophoresis analysis (Supplementary Figure S1). A similar finding was made in 50% human plasma.

**In Vitro Cell Binding.** Figure 3 shows the light-scattering, DAPI, and overlaid images of EGFR-positive OSC-19 cells incubated with apt-HAuNS, C225-HAuNS, and PEG-HAuNS. Apt-HAuNS and C225-HAuNS, both of which specifically target EGFR, exhibited a strong perinuclear signal in the cells. In contrast, few nanoparticles were seen in the cells treated with PEG-HAuNS, indicating less uptake of the nontargeted PEG-HAuNS in the cells.

**Pharmacokinetics and Biodistribution of apt-HAuNS.** To enable quantitative analysis, we labeled HAuNS conjugates with the gamma emitter  $^{111}\text{In}$ , which has a long physical half-life ( $t_{1/2} = 67.3$  h) comparable to the circulation half-life of nanoparticles.  $^{111}\text{In}$ -labeling was accomplished using 4-(aminobenzyl)diethylenetriaminepentaacetic acid thioctamide (DTPA-TA) as the radiometal chelator.

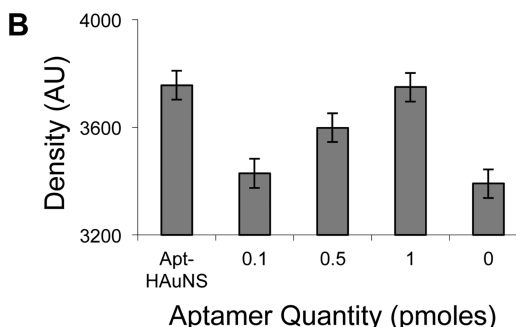
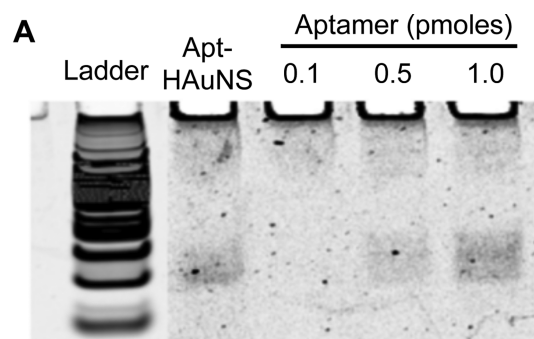


**Figure 2.** (A) Analysis of the amount of aptamers conjugated on the surface of the HAuNS. HAuNS conjugates along with control RNA samples ranging from 6 to 16 pM were loaded into a 15% denaturing PAGE gel, electrophoresed, and stained with SyBr gold. (B) Gel was imaged with a Storm Scanner (GE Life Sciences) and quantified in ImageJ, which indicates that there was  $\sim 1$  pmol of RNA per 50  $\mu\text{L}$  of HAuNS or  $\sim 250$  molecules per particle.

A previous study has shown that  $^{111}\text{In}$ -DTPA-TA labeling on the gold surface possessed excellent *in vivo* stability.<sup>18</sup> The labeling efficiency was  $\sim 70\%$ , with radiochemical purities for  $^{111}\text{In}$ -DTPA-apt-HAuNS,  $^{111}\text{In}$ -DTPA-C225-HAuNS, and  $^{111}\text{In}$ -DTPA-PEG-HAuNS greater than 95%.

Figure 4 shows blood activity–time profiles after intravenous injection of PEG-HAuNS, apt-HAuNS, and C225-HAuNS to mice. As indicated by the solid lines up to 24 h, C225-HAuNS was cleared much slower in the initial distribution period followed by a slower elimination phase as compared to PEG-HAuNS and apt-HAuNS. C225-HAuNS had almost 6-fold higher mean initial drug concentration in the blood, *i.e.*, 59.1%ID/g, as compared to 11.6%ID/g and 9.4%ID/g for PEG-HAuNS and apt-HAuNS, respectively. Pharmacokinetic parameters are presented in Table 2. C225-HAuNS has significantly higher systemic exposure/bioavailability (AUC) as compared with PEG-HAuNS and apt-HAuNS groups. The systemic clearance (CL) of C225-HAuNS was significantly slower than that of the apt-HAuNS group, which may be interpreted as the C225-HAuNS being removed less efficiently by the cells of the reticuloendothelial system. The difference in CL also resulted in the observed differences in blood half-life and mean residence time (MRT). No significance was observed between the PEG-HAuNS and C225-HAuNS groups for  $T_{1/2}$ , CL, and MRT. Also, no statistical

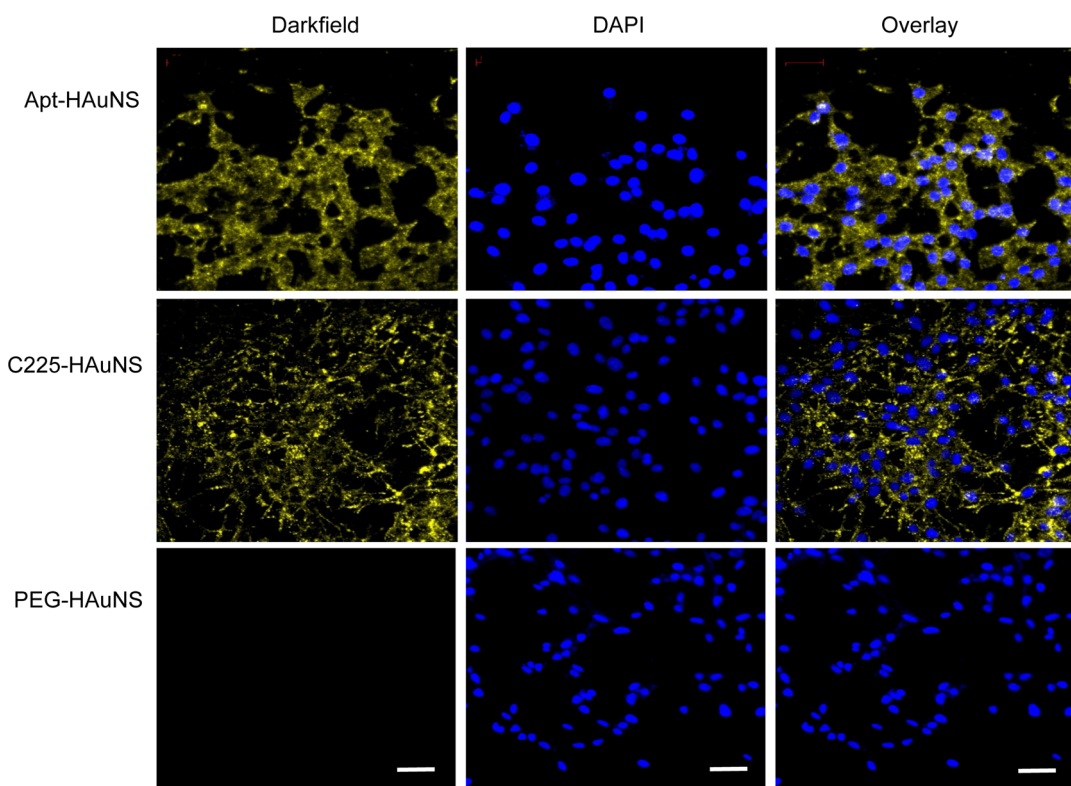


**Figure 3.** Selective binding of aptamer-coated HAuNS to OSC-19 cells. Only cells incubated with aptamer- or C225-coated HAuNS had a strong light-scattering signal. Cells were stained with DAPI for visualization of cell nuclei (blue). Light-scattering images of HAuNS were pseudocolored yellow. Bar: 50  $\mu$ m.

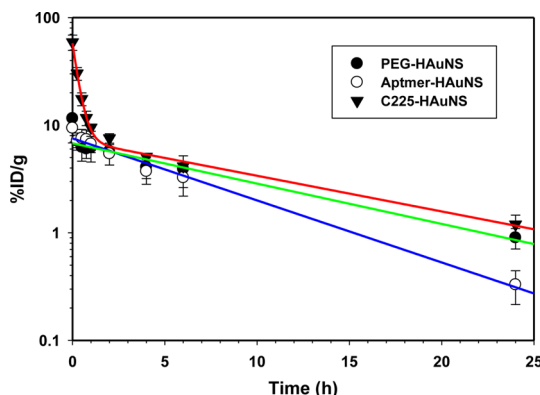


**Figure 4.** Blood activity–time profiles of  $^{111}\text{In}$ -labeled apt-HAuNS, C225-HAuNS, and PEG-HAuNS. The data are expressed as mean percentage of the injected dose per gram of blood (%ID/g)  $\pm$  standard deviation ( $n = 5$ ).

significance was observed for volume of distribution at steady-state ( $V_{ss}$ ), suggesting there is no difference in the protein- or tissue-binding properties among the three nanoparticle groups.

The biodistribution of  $^{111}\text{In}$ -labeled HAuNS conjugates at 24 h after injection was determined by ex vivo measurements of radioactivity and is presented in Table 3. The organs that had the highest uptakes of  $^{111}\text{In}$ -labeled apt-HAuNS, C225-HAuNS, and PEG-HAuNS were the spleen and the liver. Uptake levels of  $^{111}\text{In}$ -labeled apt-HAuNS and C225-HAuNS in the

liver were significantly higher than that of PEG-HAuNS. There was also significantly higher uptake of C225-HAuNS in the spleen as compared with that of PEG-HAuNS.  $^{111}\text{In}$ -labeled apt-HAuNS had a significantly higher uptake value ( $3.34 \pm 0.44\%$ ID/g) in the tumor than did  $^{111}\text{In}$ -labeled C225-HAuNS ( $1.62 \pm 0.37\%$ ID/g) or PEG-HAuNS ( $0.94 \pm 0.32\%$ ID/g). These differences were statistically significant (Tukey's test  $p < 0.001$  and 0.001, respectively) (Table 3). It is not clear why there was higher blood activity for apt-HAuNS in the tumor-bearing nude mice whereas in Swiss mice apt-HAuNS was cleared faster from the blood than PEG-HAuNS and C225-HAuNS. Probably there was a strain difference for pharmacokinetics of nanoparticles in mice. Nevertheless, our data suggest that the significant differences in tumor uptake values between apt-HAuNS and C225-HAuNS and between apt-HAuNS and PEG-HAuNS cannot be explained by enhanced permeability and retention effect or other nonspecific tumor retention mechanisms.

**In Vivo Imaging.** The presence of OSC-19 tumors in the tongues of nude mice at day 10 after inoculation was confirmed by bioluminescence imaging (Figure 5A).  $\mu$ SPECT/CT images acquired at 4 and 24 h after injection of  $^{111}\text{In}$ -labeled HAuNS conjugates are shown in Figure 5B. The imaging data confirmed the *in vivo* biodistribution data, revealing that more apt-HAuNS accumulated in the tumor than C225-HAuNS and PEG-HAuNS. Moreover, this

accumulation was higher at 24 h than at 4 h postinjection. The histologic results also confirmed the presence of HAuNS (shown as scattered yellow dots in the dark-field image in Figure 6). Apt-HAuNS, but not PEG-HAuNS, was distributed throughout the tumor matrix in the interstitial space.

Taking together pharmacokinetics, biodistribution, and imaging studies, our data support the notion that EGFR aptamer is a better tumor-homing ligand than EGFR antibody for targeted delivery of HAuNS. Clearly, additional studies in other nanoparticle systems are needed to confirm this finding. The tumor-targeting efficiency of nanoparticles is in general affected by nanoparticle size, charge, binding affinity of homing ligands to the target, and valency. Apt-HAuNS and C225-HAuNS had similar size, and both apt-HAuNS and C225-HAuNS were highly negatively charged. Therefore, size and charge are unlikely to be significant

contributing factors to the differential tumor uptake between apt-HAuNS and C225-HAuNS in the current model system. Difference in blood circulation time is also not likely a contributing factor. If the enhanced permeability and retention effect, a nonspecific uptake mechanism, played a dominant role, higher tumor uptake of C225-HAuNS as compared to apt-HAuNS should be expected, as C225-HAuNS had a longer blood half-life than apt-HAuNS did.

Future studies are needed to clarify the mechanisms of enhanced tumor delivery with aptamer *versus* antibody as homing ligands for HAuNS. Although we have measured the binding affinity for aptamer ( $K_d = 112 \text{ nM}$ ) and C225 ( $K_d = 1.69 \text{ nM}$ ) as EGFR ligands, the binding avidity of the ligand-conjugated HAuNS remains to be estimated and compared, as has been done with Herceptin-conjugated gold nanoparticles.<sup>19</sup> If C225-HAuNS shows significantly greater receptor-binding avidity than apt-HAuNS, it is possible that the “binding site barrier effect” may play a role in restricting tumor penetration of C225-HAuNS as compared to apt-HAuNS, much like what is observed with monoclonal antibodies of different binding affinity.<sup>20–22</sup> In such a case, tight binding of nanoparticles to their target cells can prevent nanoparticles from penetrating deeper into solid tumors. On the other hand, ligands

**TABLE 2. Pharmacokinetic (PK) Parameters of  $^{111}\text{In}$ -Labeled HAuNS Conjugates in Mice<sup>a</sup>**

PEG-HAuNS						
PK parameter	mouse 1	mouse 2	mouse 3	mouse 4	mouse 5	mean $\pm$ SD
AUC <sub>0-∞</sub> (%ID · h/g)	105.43	79.90	84.32	96.74	65.32	86.34 $\pm$ 15.49
T <sub>1/2</sub> (h)	9.29	8.58	9.52	7.08	11.99	9.29 $\pm$ 1.78
CL (g/h)	0.9485	1.2516	1.186	1.0337	1.531	1.1902 $\pm$ 0.23
V <sub>ss</sub> (g)	10.90	12.48	13.91	8.51	22.06	13.57 $\pm$ 5.15
MRT (h)	11.49	9.97	11.73	8.24	14.41	11.17 $\pm$ 2.29
Aptmer-HAuNS						
PK parameter	mouse 1	mouse 2	mouse 3	mouse 4	mouse 5	mean $\pm$ SD
AUC <sub>0-∞</sub> (%ID · h/g)	45.35	67.54	90.16	64.04	57.17	64.85 $\pm$ 16.49
T <sub>1/2</sub> (h)	5.62	4.95	5.80	6.84	5.17	5.68 $\pm$ 0.73 <sup>b</sup>
CL (g/h)	2.2052	1.4805	1.1092	1.5616	1.7493	1.6212 $\pm$ 0.40
V <sub>ss</sub> (g)	13.62	8.15	7.43	11.39	10.13	10.14 $\pm$ 2.50
MRT (h)	6.17	5.50	6.70	7.29	5.79	6.29 $\pm$ 0.72 <sup>b</sup>
C225-HAuNS						
PK parameter	mouse 1	mouse 2	mouse 3	mouse 4	mouse 5	mean $\pm$ SD
AUC <sub>0-∞</sub> (%ID · h/g)	108.63	120.45	139.31	108.29	119.17	114.57 <sup>c,d</sup>
T <sub>1/2</sub> (h)	9.10	9.60	11.48	8.73	9.73	9.73 $\pm$ 1.22 <sup>d</sup>
CL (g/h)	0.9205	0.8303	0.7178	0.9234	0.848	0.848 $\pm$ 0.0970 <sup>d</sup>
V <sub>ss</sub> (g)	8.79	8.37	8.97	8.30	8.61	8.61 $\pm$ 0.32
MRT (h)	9.54	10.08	12.49	8.99	10.28	10.28 $\pm$ 1.54 <sup>d</sup>

<sup>a</sup> AUC: area under the curve; T<sub>1/2</sub>: terminal elimination half-life; CL: systemic clearance; V<sub>ss</sub>: volume of distribution at steady state; MRT: mean residence time.

<sup>b</sup> Significantly different between PEG-HAuNS and apt-HAuNS groups. <sup>c</sup> Significantly different between PEG-HAuNS and C225-HAuNS groups. <sup>d</sup> Significantly different between apt-HAuNS and C225-HAuNS groups.

**Figure 5. Selective uptake of apt-HAuNS in orthotopic OSC-19 tumors. (A) Optical images of mice confirming the presence of tumors in the tongue. (B) Representative  $\mu\text{SPECT}/\text{CT}$  images of mice after intravenous injection of  $^{111}\text{In}$ -labeled apt-HAuNS, C225-HAuNS, or PEG-HAuNS. Arrows: tumor.**

**TABLE 3. Biodistribution of DTPA- $^{111}\text{In}$ -Labeled HAuNS Conjugates in Nude Mice 1 Day after Injection<sup>a</sup>**

	blood	liver	spleen	kidney	muscle	lymph node	tongue	tumor
Apt-HAuNS	1.56 $\pm$ 1.60	16.76 $\pm$ 9.22 <sup>b</sup>	39.00 $\pm$ 3.83	1.18 $\pm$ 1.37	0.09 $\pm$ 0.09	2.77 $\pm$ 2.60	1.83 $\pm$ 1.74	3.34 $\pm$ 0.50 <sup>b,d</sup>
C225-HAuNS	0.60 $\pm$ 0.22	19.50 $\pm$ 1.00 <sup>c</sup>	45.46 $\pm$ 17.85 <sup>c</sup>	0.70 $\pm$ 0.12	0.04 $\pm$ 0.02	0.86 $\pm$ 0.29	0.83 $\pm$ 0.18	1.62 $\pm$ 0.37
PEG-HAuNS	1.06 $\pm$ 0.50	5.71 $\pm$ 0.62	23.60 $\pm$ 1.72	0.66 $\pm$ 0.03	0.10 $\pm$ 0.01	1.15 $\pm$ 0.30	1.83 $\pm$ 1.20	0.94 $\pm$ 0.32

<sup>a</sup> Data were plotted as percentage of injected dose per gram of tissue (% ID/g). Mean  $\pm$  SD ( $n = 5$ ); \* $p < 0.05$ ; \*\* $p < 0.01$ . <sup>b</sup> Significantly different between Aptmer-HAuNS and PEG-HAuNS groups. <sup>c</sup> Significantly different between C225-HAuNS and PEG-HAuNS groups. <sup>d</sup> Significantly different between Aptmer-HAuNS and C225-HAuNS groups.

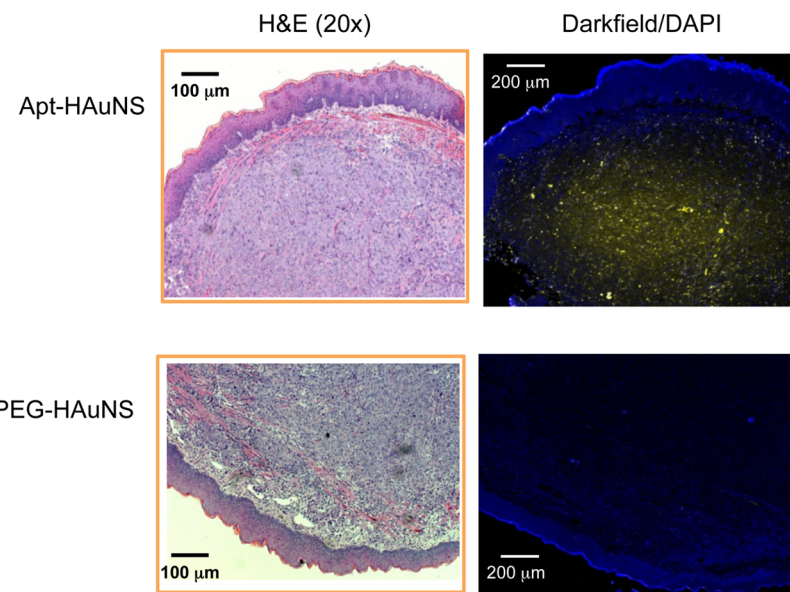


**Figure 6.** Representative photomicrographs of sectioned OSC-19 tumors from mice injected intravenously with apt-HAuNS or PEG-HAuNS. For histologic examination, sections were stained with hematoxylin and eosin. For dark-field imaging of the scattering signal (yellow) from HAuNS, cell nuclei were stained with DAPI (blue). Apt-HAuNS, but not PEG-HAuNS, was found distributed throughout the tumor matrix.

with moderate binding affinity can be released from their first encountered cellular targets and penetrate deeper into the tumor, leading to higher tumor uptake.

## CONCLUSION

In this study, we compared the pharmacokinetics, biodistribution, and imaging properties of aptamer- and antibody-conjugated HAuNS and evaluated their specific targeting to EGFR-positive cells. Surface

coating of HAuNS did not significantly alter the physicochemical properties or pharmacokinetics of the nanoparticles. The selectivity of apt-HAuNS toward EGFR-positive cells was shown both *in vitro* and *in vivo* and was confirmed by *ex vivo* microscopic evaluation. Our results indicate that aptamer directed to EGFR is a promising ligand for targeted delivery of HAuNS for selective thermal ablation of head and neck cancers overexpressing EGFR.

## MATERIALS AND METHODS

**Materials.** Common reagents were purchased from Sigma-Aldrich (St. Louis, MO, USA) or Acros (Geel, Belgium) and were used as received unless otherwise specified. Methoxy-sulfohydro-PEG (SH-PEG, molecular weight 5000) was obtained from Sigma-Aldrich. The monoclonal anti-EGFR antibody C225 was obtained from ImClone Systems (New York, NY, USA). C225 is a chimeric human–mouse immunoglobulin G1 that binds EGFR with high affinity.<sup>23,24</sup> Recombinant human EGFR/ErbB1 Fc chimera (rhEGF) was obtained from R&D Systems (Minneapolis, MN, USA). Tris(2-carboxyethyl)phosphine was purchased from Pierce Biotechnology (Rockford, IL, USA). NAP-5 columns were obtained from GE Healthcare (Illustra, Buckinghamshire, UK). Indium-111 chloride (<sup>111</sup>InCl<sub>3</sub>) was obtained from Perkin–Elmer (Waltham, MA, USA). Isoflurane was obtained from Henry Schein Animal Health (formerly Butler Animal Health Supply, Dublin, OH, USA). All the chemicals and solvents were at least American Chemical Society grade and were used without further purification.

**Synthesis of HAuNS and Its Conjugates.** HAuNS was synthesized according to our previously published method.<sup>8</sup> Briefly, cobalt nanoparticles were first synthesized by deoxygenating deionized water containing sodium borohydride (4.5 mL, 1 mol/L), sodium citrate (2.8 mL, 0.1 mol/L), and cobalt chloride (1.0 mL, 0.4 mol/L). The cobalt nanoparticle solution was then added to chloroauric acid, resulting in reduction of gold ions onto the surface of cobalt nanoparticles and oxidation of cobalt to cobalt oxide. Any remaining cobalt core was oxidized by air, producing the final product, HAuNS.

For apt-HAuNS synthesis, a 5' thiol-modified DNA at the C6 position (5'ThioMC6-D/TGGTCATGGC GGGCATTAATT, Integrated DNA Technologies, Coralville, IA, USA) was deprotected using tris(2-carboxyethyl)phosphine and then purified by NAP-5 columns per the manufacturer's instructions. A large volume of HAuNS (500 μL; 3.35 × 10<sup>12</sup> particles/mL; 50 OD) was added to 10 μL (16 μM) of deprotected oligonucleotide in water at 80 °C. The HAuNS were allowed to cool to 25 °C and then centrifuged at 8000g for 10 min and washed with water twice to remove any unreacted oligonucleotide. To these DNA-coated HAuNS, 16 pmol of 2'-fluoropyrimidine-modified RNA, 5'-GGC GCU CCG ACC UUA GUC UCU GUG CCG CUA UAA UGC ACG GAU UUA AUC GCC GUA GAA AAG CAU GUC AAA GCC GGA ACC GUG UAG CAC AGC AGA GAAUAAAUGCCGCAUGACCAG-3' (E07,<sup>25</sup> with underlined letters as the complementary sequence), which was kindly provided by Dr. Andrew Ellington from University of Texas in Austin, was added and annealed at 80 °C for 3 min. This sample was again centrifuged at 8000g for 10 min and washed with water twice to remove any uncaptured RNA. To ensure complete coverage of gold surface, PEG-SH (MW = 5000) was added to the apt-coated HAuNS to a final concentration of 0.2 mg/mL, and the mixture was reacted for an additional 1 h. After the washing steps, the resulting apt-HAuNS was resuspended in 0.1 M phosphate-buffered saline (PBS).

C225- and PEG-conjugated HAuNS (C225-HAuNS and PEG-HAuNS, respectively) were prepared according to a previously published protocol.<sup>8</sup> Briefly, an aqueous solution of C225 (2.5 mg; 0.017 μmol; 5 mg/mL) was first allowed to react with *N*-succinimidyl-5-acetylthioacetate (SATA) (0.077 mg; 0.332 μmol)

at room temperature for 1 h. The resulting conjugate, C225-acetylthioacetate (C225-ATA), was purified by passing it through a gel filtration PD-10 column, and Biorad protein assay dye reagent (BioRad, Hercules, CA, USA) was used to guide the collection of antibody-containing fractions. C225-ATA was treated with hydroxylamine (50 mM; 50  $\mu$ L) at room temperature for 2 h to expose the free thiol (SH) group. The reaction mixture was passed through a PD-10 column, and the resulting C225-SH was added to an aqueous solution of HAuNS ( $1.4 \times 10^{12}$  particles/mL, 20 OD) for a final antibody concentration of 5  $\mu$ g/mL. The suspension was stirred at room temperature for 1 h. Thereafter, PEG-SH (MW = 5000) was added to the antibody-coated HAuNS to a final concentration of 0.2 mg/mL, and the mixture was reacted for an additional 1 h to ensure that the gold surface in C225-HAuNS was completely covered with PEG. C225-HAuNS were centrifuged at 8000g for 5 min, and the resulting pellet was washed twice with deionized water to remove any unattached C225 and PEG from the supernatant. The purified product was resuspended in 0.1 mM PBS and stored at 4 °C until further use. C225-HAuNS were stable in physiological buffers for at least 3 weeks at 4 °C without aggregation.

**Characterization of HAuNS Conjugates.** The particle size was determined using dynamic light scattering at a scatter angle of 90° on a Brookhaven particle size analyzer (Holtsville, NY, USA). Ultraviolet (UV)-visible spectroscopy was recorded on a Beckman Coulter UV-visible spectrometer (Indianapolis, IN, USA).

To quantify the amount of aptamer conjugated on the surface of the HAuNS, apt-HAuNS along with control RNA samples ranging from 6 to 16 pM were loaded into a 15% denaturing PAGE gel, electrophoresed, and stained with SyBr gold according to the manufacturer's recommendation (Invitrogen, Eugene, OR, USA). The gel was imaged with a Storm Scanner (GE Life Sciences, Piscataway, NJ, USA), and free RNA in the HAuNS sample was quantified in ImageJ by taking the average intensity value within the band (after background subtraction). The control sample was used as a reference and taken to represent the total loaded RNA.

SPR binding assays were performed with a Biacore 3000 model system (GE Healthcare, Piscataway, NJ, USA) at 25 °C using HBSEP running buffer (0.01 M HEPES [4-(2-hydroxyethyl)-1-piperazineethanesulfonic acid], pH 7.4, 0.15 M NaCl, 3 mM ethylenediaminetetraacetic acid, and 0.005% [v/v] surfactant P20 solution). A CM-5 chip was successfully coated with recombinant human EGFR/ErbB1 Fc chimera using the 1-ethyl-3-(3-(dimethylamino)propyl)carbodiimide/N-hydroxysuccinimide (EDC/NHS method). The EGFR aptamer and C225 were diluted in HBSEP buffer, filtered, degassed, and injected at a flow rate of 30  $\mu$ L/min as a series of eight concentrations. The injection time of aptamer and C225 in the HBSEP buffer was 7 min, followed by a 3 min dissociation period. The CM-5 chips were regenerated using a 30 s pulse of 10 mM glycine (pH 2.2) after each binding cycle. All analyzed samples and running buffer were injected to an rhEGFR-coated flow cell and uncoated reference cell. Data were evaluated using BIAevaluation software, version 3.1 (GE Healthcare). The obtained sensograms were fitted globally over the whole range of injected concentrations and simultaneously over the association and dissociation phases. Equilibrium dissociation constants were then calculated from the rate constants ( $K_d = k_{off}/k_{on}$ ).

**Radiolabeling.**  $^{111}\text{In}$ -chelate complex was prepared ahead of time by dissolving 4-aminobenzyl-diethylenetriaminepentaacetic acid thiocarbamate [DTPA-TA, 10  $\mu$ g] in 0.1 M sodium acetate solution (pH 5.2) and then adding [1 mCi, 1 mL]  $^{111}\text{InCl}_3$  and reacting for 30 min at room temperature. DTPA-TA was synthesized according to previously reported procedures.<sup>18</sup> Radiolabeling of apt-HAuNS, C225-HAuNS, and PEG-HAuNS was achieved by mixing aliquots of each nanoparticle preparation with  $^{111}\text{In}$ -chelate and rotating it overnight at 4 °C. The next day, 0.2  $\mu$ g/mL of PEG-SH was added to the solution, which was then rotated for an additional 2 h to stabilize the radiolabeled HAuNS conjugates. Unlabeled  $^{111}\text{In}$  and  $^{111}\text{In}$ -DTPA-aptamer and -antibody were removed by centrifugation and washing steps. The radiolabeled nanoparticles were analyzed using an instant thin-layer chromatography strip developed with PBS (pH 7.4)

containing 4 mM ethylenediaminetetraacetic acid. The data were quantified using a Bioscan IAR-2000 TLC scanner (Washington, DC, USA). Free  $^{111}\text{In}^{3+}$  ions moved to the solvent front ( $R_f = 0.9$ ), and the nanoparticles remained in their original location ( $R_f = 0.0$ ).

**In Vitro Cell Binding.** The EGFR-positive oral squamous cell carcinoma cell line OSC-19<sup>26,27</sup> was kindly provided by Dr. Jeffrey Myers (The University of Texas MD Anderson Cancer Center). OSC-19 cells were maintained at 37 °C in a humidified atmosphere containing 5% CO<sub>2</sub> in Dulbecco's modified Eagle's medium and nutrient mixture F-12 Ham containing 10% fetal bovine serum (Invitrogen, Grand Island, NY, USA).

For microscopic imaging to assess *in vitro* binding, OSC-19 cells were seeded onto an eight-well Lab-Tek II chamber slide (10 000 cells/well) (Thermo Scientific, Rochester, NY, USA). After 24 h, the cells were washed three times with Hank's balanced salt solution and incubated with apt-HAuNS, C225-HAuNS, and PEG-HAuNS (100  $\mu$ L,  $1 \times 10^{11}$  particles/mL) at 37 °C for 1 h. Thereafter, the cells were washed three times with Hank's balanced salt solution and fixed with 70% ethanol for 30 min. The cell nuclei were stained with 4',6'-diamidino-2-phenylindole (DAPI) for 5 min. Cells were then washed three times with PBS, mounted, and examined under a Zeiss Axio Observer.Z1 fluorescence microscope (Carl Zeiss MicroImaging GmbH, Göttingen, Germany). HAuNS were examined under a dark-field condenser illuminated by a halogen light source, and the fluorescence of the cell nuclei was detected with a Chroma DAPI filter (Chroma Technology Corp., Bellows Falls, VT, USA) illuminated by a Xenon XBO light source (OSRAM GmbH, Augsburg, Germany). The images were collected using a Hamamatsu B/W chilled charge-coupled camera (Hamamatsu Photonics K. K., Hamamatsu City, Japan) and processed using Image-Pro Plus 4.5.1 software (Media Cybernetics, Inc., Bethesda, MD, USA). The dark-field condenser allows imaging scattered light from HAuNS.

**Pharmacokinetic Study.** All animal studies were carried out in the Small Animal Imaging Facility at MD Anderson Cancer Center in accordance with institutional guidelines and approved by the IACUC. For the pharmacokinetic study, healthy male Swiss mice (22–25 g; Charles River Laboratories, Wilmington, MA, USA) ( $n = 4$ –5/group) were injected intravenously with  $^{111}\text{In}$ -labeled apt-HAuNS and PEG-HAuNS at a dose of  $7.3 \times 10^{11}$  particles/mouse (1.4 mg HAuNS/kg body weight; 10 OD HAuNS; 30  $\mu$ Ci/mouse; 200  $\mu$ L/mouse). At predetermined intervals (0 min, 15 min, 30 min, 45 min, 1 h, 2 h, 4 h, 6 h, and 24 h), blood samples (10  $\mu$ L) were taken from the tail vein, and the radioactivity of each sample was measured with a Cobra Auto-gamma counter (Packard, Downers Grove, IL, USA).

All pharmacokinetic analyses were made using classical techniques and the microcomputer-based program Phoenix WinNonlin 6.3 software (Pharsight Corp., St. Louis, MO, USA). The HAuNS blood concentration–time data were interpreted by noncompartmental methods. The total area under the blood concentration–time curve ( $AUC_{0-\infty}$ ) and the area under the first moment of the blood concentration–time curve (AUMC) were estimated by the trapezoidal rule with extrapolation of the terminal portion to infinity. The rate constant ( $K$ ) governing the terminal elimination of the gold nanoparticles from the body was determined from the least-squares slope of the terminal linear segment of a semilogarithmic plot of blood gold nanoparticle concentration *versus* time. The elimination half-life ( $T_{1/2}$ ) was calculated as  $0.693/K$ . The systemic clearance was determined from dose/AUC. The volume of distribution at steady state was calculated using the following formula: Dose/[ $(\text{AUMC})/(\text{AUC}^2)$ ]. The mean residence time was calculated from AUMC/AUC.

Statistical analyses were conducted using SYSTAT 11 (SYSTAT Inc., Evanston, IL, USA). Prior to the application of any statistical test, the Levene's test for equality of variance was performed on the variances of the observations in the individual nanoparticle groups. Since we found that all the data from the three groups was homogeneous, the analysis of variance (ANOVA) followed by *post hoc* Tukey's test was used to determine the statistical significance among the groups. A *p*-value of less than 0.05 was considered as statistically significant.

**Imaging and Biodistribution Studies.** An orthotopic oral squamous cell carcinoma model was created by injecting OSC-19-Luc cells ( $5.0 \times 10^4$  cells/mouse) into the tongues of 6- to 8-week-old male nude mice. Two weeks after cell inoculation (tumor size is approximately  $3 \times 5 \times 2$  mm), luciferin (150 mg/kg) was injected intraperitoneally, and chemiluminescence optical imaging was performed with a Xenogen IVIS 200 optical imaging system (Hopkinton, MA, USA) to confirm tumor formation. Tumor-bearing mice were randomly divided into three groups ( $n = 5$  mice/group) and intravenously injected with  $^{111}\text{In}$ -labeled apt-HAuNS, C225-HAuNS, or PEG-HAuNS. At 4 and 24 h after administration of the nanoparticle preparation,  $\mu$ SPECT/CT images were acquired using a Gamma Medica  $\mu$ SPECT-CT scanner (Northridge, CA, USA). SPECT scans (radius of rotation = 3 cm; 32 projections; 20 s per projection) and CT scans (512 projections; 75 kV; 500 mA) were acquired and coregistered for image fusion and presentation of three-dimensional anatomical localization of the tracer signal. Acquired SPECT and CT data sets were processed using AMIRA 5.1 software (San Diego, CA, USA). During each imaging session, mice were anesthetized with 2% isoflurane gas in oxygen.

After the imaging was completed, the mice were killed immediately. The tumors and various other tissues were removed, weighed, and assessed for radioactivity using a Cobra Autogamma counter. Uptake of the nanoparticles was calculated as the percentage of the injected dose per gram of tissue (%ID/g). Student's *t* test was used to compare differences in tissue uptake between the different groups, and *p*-values less than 0.05 were considered significant.

**Histology.** Tumors harvested at the end of the imaging session were snap-frozen and cut into 5  $\mu\text{m}$  sections. One of the slides was stained for hematoxylin and eosin, while an adjacent slide was counterstained with DAPI for fluorescence and dark-field imaging. Images were recorded using a Zeiss Axio Observer.Z1 fluorescence microscope equipped with a UV filter for DAPI and a dark-field condenser.

**Conflict of Interest:** The authors declare no competing financial interest.

**Acknowledgment.** We thank D. Chalaire for editing the manuscript. This work was supported in part by grants from the National Institutes of Health (U54CA151668), an Odyssey Fellowship (to M.P.M.), a SPORE Head and Neck Career Development Award (to M.P.M.), and the John S. Dunn Foundation. The work on the EGFR aptamer was funded by the National Institutes of Health (EUREKA, 1-R01-GM094933), The Welch Foundation (F-1654), and a National Security Science and Engineering Faculty Fellowship (FA9550-10-1-0169).

**Supporting Information Available:** A detailed description of the stability of aptamer–HAuNS complex in mouse plasma using gel electrophoresis is available free of charge via the Internet at <http://pubs.acs.org>.

## REFERENCES AND NOTES

- Lu, W.; Melancon, M. P.; Xiong, C. Y.; Huang, Q.; Elliott, A.; Song, S. L.; Zhang, R.; Flores, L. G.; Gelovani, J. G.; Wang, L. H. V.; et al. Effects of Photoacoustic Imaging and Photothermal Ablation Therapy Mediated by Targeted Hollow Gold Nanospheres in an Orthotopic Mouse Xenograft Model of Glioma. *Cancer Res.* **2011**, *71*, 6116–6121.
- Lu, W.; Huang, Q.; Geng, K. B.; Wen, X. X.; Zhou, M.; Guzatov, D.; Brecht, P.; Su, R.; Oraevsky, A.; Wang, L. V.; et al. Photoacoustic Imaging of Living Mouse Brain Vasculature Using Hollow Gold Nanospheres. *Biomaterials* **2010**, *31*, 2617–2626.
- You, J.; Zhang, R.; Xiong, C.; Zhong, M.; Melancon, M.; Gupta, S.; Nick, A. M.; Sood, A. K.; Li, C. Effective Photothermal Chemotherapy Using Doxorubicin-Loaded Gold Nanospheres That Target Ephb4 Receptors in Tumors. *Cancer Res.* **2012**, *72*, 4777–4786.
- Huang, X. H.; Jain, P. K.; El-Sayed, I. H.; El-Sayed, M. A. Plasmonic Photothermal Therapy (Pptt) Using Gold Nanoparticles. *Laser Med. Sci.* **2008**, *23*, 217–228.
- Melancon, M. P.; Zhou, M.; Li, C. Cancer Theranostics with near-Infrared Light-Activatable Multimodal Nanoparticles. *Acc. Chem. Res.* **2011**, *44*, 947–956.
- Zhao, N.; You, J.; Zeng, Z.; Li, C.; Zu, Y. An Ultra Ph-Sensitive and Aptamer-Equipped Nanoscale Drug-Delivery System for Selective Killing of Tumor Cells. *Small* **2013**, *9*, 3477–3484.
- Lu, W.; Xiong, C.; Zhang, G.; Huang, Q.; Zhang, R.; Zhang, J. Z.; Li, C. Targeted Photothermal Ablation of Murine Melanomas with Melanocyte-Stimulating Hormone Analog-Conjugated Hollow Gold Nanospheres. *Clin. Cancer Res.* **2009**, *15*, 876–886.
- Melancon, M. P.; Lu, W.; Yang, Z.; Zhang, R.; Cheng, Z.; Elliot, A. M.; Stafford, J.; Olson, T.; Zhang, J. Z.; Li, C. *In Vitro* and *in Vivo* Targeting of Hollow Gold Nanoshells Directed at Epidermal Growth Factor Receptor for Photothermal Ablation Therapy. *Mol. Cancer Ther.* **2008**, *7*, 1730–1739.
- Lu, W.; Zhang, G.; Zhang, R.; Flores, L. G., 2nd; Huang, Q.; Gelovani, J. G.; Li, C. Tumor Site-Specific Silencing of Nf-Kappab P65 by Targeted Hollow Gold Nanosphere-Mediated Photothermal Transfection. *Cancer Res.* **2010**, *70*, 3177–3188.
- Ng, E. W.; Adamis, A. P. Targeting Angiogenesis, the Underlying Disorder in Neovascular Age-Related Macular Degeneration. *Can. J. Ophthalmol.* **2005**, *40*, 352–368.
- Lee, J. F.; Stovall, G. M.; Ellington, A. D. Aptamer Therapeutics Advance. *Curr. Opin. Chem. Biol.* **2006**, *10*, 282–289.
- Hu, M.; Zhang, K. The Application of Aptamers in Cancer Research: An up-to-Date Review. *Future Oncol.* **2013**, *9*, 369–376.
- Barbas, A. S.; Mi, J.; Clary, B. M.; White, R. R. Aptamer Applications for Targeted Cancer Therapy. *Future Oncol.* **2010**, *6*, 1117–1126.
- Mendelsohn, J.; Baselga, J. Status of Epidermal Growth Factor Receptor Antagonists in the Biology and Treatment of Cancer. *J. Clin. Oncol.* **2003**, *21*, 2787–2799.
- Bonner, J. A.; De Los Santos, J.; Waksal, H. W.; Needle, M. N.; Trummel, H. Q.; Raisch, K. P. Epidermal Growth Factor Receptor as a Therapeutic Target in Head and Neck Cancer. *Semin. Radiat. Oncol.* **2002**, *12*, 11–20.
- Ang, K. K.; Berkey, B. A.; Tu, X.; Zhang, H. Z.; Katz, R.; Hammond, E. H.; Fu, K. K.; Milas, L. Impact of Epidermal Growth Factor Receptor Expression on Survival and Pattern of Relapse in Patients with Advanced Head and Neck Carcinoma. *Cancer Res.* **2002**, *62*, 7350–7356.
- Dassonville, O.; Formento, J. L.; Francoual, M.; Ramaioli, A.; Santini, J.; Schneider, M.; Demand, F.; Milano, G. Expression of Epidermal Growth Factor Receptor and Survival in Upper Aerodigestive Tract Cancer. *J. Clin. Oncol.* **1993**, *11*, 1873–1878.
- Zhang, G.; Yang, Z.; Lu, W.; Zhang, R.; Huang, Q.; Tian, M.; Li, L.; Liang, D.; Li, C. Influence of Anchoring Ligands and Particle Size on the Colloidal Stability and *in Vivo* Biodistribution of Polyethylene Glycol-Coated Gold Nanoparticles in Tumor-Xenografted Mice. *Biomaterials* **2009**, *30*, 1928–1936.
- Jiang, W.; Kim, B. Y.; Rutka, J. T.; Chan, W. C. Nanoparticle-Mediated Cellular Response Is Size-Dependent. *Nat. Nanotechnol.* **2008**, *3*, 145–150.
- Adams, G. P.; Schier, R.; McCall, A. M.; Simmons, H. H.; Horak, E. M.; Alpaugh, R. K.; Marks, J. D.; Weiner, L. M. High Affinity Restricts the Localization and Tumor Penetration of Single-Chain Fv Antibody Molecules. *Cancer Res.* **2001**, *61*, 4750–4755.
- Fujimori, K.; Covell, D. G.; Fletcher, J. E.; Weinstein, J. N. A Modeling Analysis of Monoclonal Antibody Percolation through Tumors: A Binding-Site Barrier. *J. Nucl. Med.* **1990**, *31*, 1191–1198.
- Chames, P.; Van Regenmortel, M.; Weiss, E.; Baty, D. Therapeutic Antibodies: Successes, Limitations and Hopes for the Future. *Br. J. Pharmacol.* **2009**, *157*, 220–233.
- Mendelsohn, J. Epidermal Growth Factor Receptor Inhibition by a Monoclonal Antibody as Anticancer Therapy. *Clin. Cancer Res.* **1997**, *3*, 2703–2707.
- Goldstein, N. I.; Prewett, M.; Zuklys, K.; Rockwell, P.; Mendelsohn, J. Biological Efficacy of a Chimeric Antibody to

- the Epidermal Growth Factor Receptor in a Human Tumor Xenograft Model. *Clin. Cancer Res.* **1995**, *1*, 1311–1318.
25. Li, N.; Nguyen, H. H.; Byrom, M.; Ellington, A. D. Inhibition of Cell Proliferation by an Anti-EGFR Aptamer. *PLoS One* **2011**, *6*, e20299.
26. Sano, D.; Choi, S.; Milas, Z. L.; Zhou, G.; Galer, C. E.; Su, Y. W.; Gule, M.; Zhao, M.; Zhu, Z.; Myers, J. N. The Effect of Combination Anti-Endothelial Growth Factor Receptor and Anti-Vascular Endothelial Growth Factor Receptor 2 Targeted Therapy on Lymph Node Metastasis: A Study in an Orthotopic Nude Mouse Model of Squamous Cell Carcinoma of the Oral Tongue. *Arch. Otolaryngol. Head Neck Surg.* **2009**, *135*, 411–420.
27. Sano, D.; Matsumoto, F.; Valdecanas, D. R.; Zhao, M.; Molkentin, D. P.; Takahashi, Y.; Hanna, E. Y.; Papadimitrakopoulou, V.; Heymach, J.; Milas, L.; et al. Vandetanib Restores Head and Neck Squamous Cell Carcinoma Cells' Sensitivity to Cisplatin and Radiation *in Vivo* and *in Vitro*. *Clin. Cancer Res.* **2011**, *17*, 1815–1827.